AUT Journal of Electrical Engineering
10.22060/EEJ.2026.24622.5737

# Grid-Integrated Solar EV Charging Station with Double Stage Coupled Inductor Boost Converter and Artic Puffin Optimized PI Control

Sivaprasad Kollati[1*], Saritha Kandukuri[2], Singamsetti Mohan Santhi[3], Nishu Kumar[4], Santhosh Kumar Magapu[5]

[1]Assistant Professor, Department of Electrical and Electronics Engineering, Godavari Global University, Rajahmundry, India.
[2]Assistant Professor, Department of Electrical and Electronics Engineering, Godavari Institute of Engineering and Technology (A), Rajahmundry, India.
[3, 4, 5] UG Scholar, Department of Electrical and Electronics Engineering Godavari Institute of Engineering and Technology (A), India.

*Corresponding author: ksivaprasad22@gmail.com

**Abstract:**

Environmental benefits of Electric Vehicles (EVs) are associated with reduction of direct air pollutants and reduction of greenhouse gases. In this paper, a novel solar-powered EV Charging Station (EVCS) is offered with the integration of a grid-based energy management system and a high-efficiency Double-Stage Coupled Inductor Boost Converter (DSCIB). A new Arctic Puffin Optimized (APO) Proportional-Integral (PI) controller is employed for preserving a constant DC-link voltage and optimal system performance. This approach optimizes the energy transfer efficiency and enhances a stability under dynamic operating conditions. DC bus is linked to electrical grid through LC filter and three phase Voltage Source Inverter (VSI), which allows bidirectional power flow and reactive power support. PI-based control loop is employed for grid synchronization, to properly balance the active and reactive power. The charging and discharging processes of EV battery are controlled via a bidirectional DC-DC (BDC) converter, which is structured with the PI control strategy to precisely control the voltage and current. This configuration offers the capability of battery-to-grid without any interruption and fast charging of EV batteries during excess PV generation. The MATLAB simulation results shows proposed architecture offers a promising option for sustainable EV integration in grid applications because of the coordinated control framework. From simulation converter attain efficiency of 98.4% and decrease THD of 1.02% ensure effective energy flow, voltage stability, and grid support.

AUT Journal of Electrical Engineering
10.22060/EEJ.2026.24622.5737

**Keywords:**

Photovoltaic system, Double Stage Coupled Inductor Boost Converter, Arctic Puffin Optimization Algorithm, PI controller, grid application.

## 1. Introduction

Fossil fuels, which are used mainly for the production of electricity, dominate the imported energy products. Combustion of them has colossal environmental impacts, such as releasing immense amounts of Greenhouse Gases (GHGs) and other toxic pollutants. The emissions lead to acid rain and respiratory disease in human beings. Additionally, Carbon Dioxide ($CO_2$) emissions lead to global warming and climatic changes [1]. Electric-powered vehicles present a compelling substitute for fossil-fuel-driven automobiles in today's automotive sector [2]. Renewable energy systems are increasingly being used worldwide today in response to increasing energy demand and environmental pollution. RES offers a clean alternative, which produce electricity without fuel combustion or the emission of toxic pollutants, thereby facilitating the shift away from fossil fuels [3].

To maximize the utilization of renewable power, integration with the utility grid is essential. Among renewable energy technologies, grid-connected PV systems have experienced the fastest growth, largely due to its efficiency, compactness, weight reduction, reliability, and ease of installation have significantly improved inverter performance and cost-effectiveness [4]. Grid-connected PV system is much efficient operation because of the power generated is supplied to the power grid for instantaneous transmission, distribution, and utilization, here, energy storage is not required. This solution also reduces the burden on other energy sources that power the grid [5].

For an EVCS, PV output is frequently low. To interface it with grid, a high step-up DC-DC converter is utilized at front end to step up and regulate this voltage to the DC bus specifications. There have been numerous voltages boosting techniques used in step-up converters [6]. Traditional boost converter attains a high voltage gain through working at a duty cycle approaching unity. However, this typically leads to significant conduction losses, which represent a major limitation of this configuration [7]. The buck–boost architecture is realized by cascading a buck converter and a boost converter. When both switches operate with same duty cycle, overall voltage conversion ratio is product of each stage's individual ratio. Specifically, employing a buck converter yields a cascaded buck–boost configuration, effectively extending the converter's functionality through a wider range of input and output voltages. Nevertheless, converter configuration exhibits high input-voltage ripple and high electrical switch stresses [8]. Another possible voltage enhancing approach to step-up voltage level of DC-DC converters is retaining coupled magnetics. High frequency transformers are utilized to balance input voltage with additional lead of delivering electrical isolation. Though, these converters deliver greater voltage gain than traditional boost converter, however these converters necessity a higher amount of components with multi-level/stage solutions. This, naturally, effects a greater difficulty, expense and reduces efficacy and power density [9-10]. As, a result this research proposes a DSCIB converter that maximize voltage gain while minimizing losses and component stress.

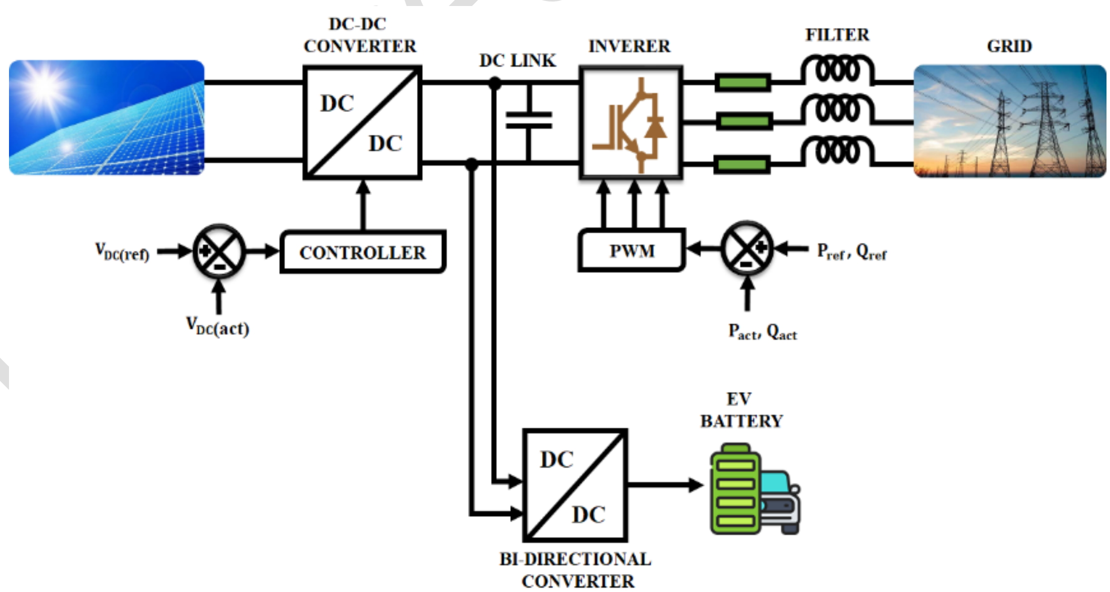


Fig. 1. Structure grid-connected PV systems

10.22060/EEJ.2026.24622.5737

Fig. 1 displays the schematic workflow of proposed grid-integrated PV system. Power managed from PV system is improved via DC converter, nevertheless, its switching operations are further controlled by a dynamic control mechanism that responds to real-time fluctuations in solar irradiance and grid demand [11-12]. Two common control approaches in PV systems are the MPPT controllers and the PI controllers. MPPT techniques are mostly used to extract maximum power from PV arrays. However, performance of these techniques is affected by tracking oscillations and rapidly fluctuations in the environment. To maintain DC-link voltage directive and system stability. Hence, PI controller is adopted because of its fast response, less overshoot and better dynamic performance. PI controllers have long been favoured in grid-connected PV systems for regulating system parameters under various disturbances. Though, their performance gets significantly improved through the adoption of optimization algorithms [13]. Genetic Algorithm (GA) is a popular revolutionary algorithm for solving complex search and optimization problems, inspired by natural selection process is implemented for effective tuning of the PI controller parameters [14]. Bacterial Foraging Optimization Algorithm (BFOA) mimics the behaviour of E. coli bacteria foraging for nutrients, identifies optimal parameter settings $K_p$ and $K_i$ gain values by continuously improving solutions through bio-inspired steps [15]. Particle Swarm Optimization (PSO) algorithm for tuning parameters of PI controller has been preconfigured for identifying optimal controller settings. Integral Squared Error (ISE) serves as objective function, derived from discrepancy between the input and output signals at each iteration, the highest computed value is used to update the solution for the subsequent stage. Although these conventional optimization algorithms exhibits a higher peak overshoot, along with a higher minimum cost function value [16].

Growing demand for sustainable EVCS results in the creation of effective renewable energy-based solutions. Existing high gain converters and controller optimization methods are often plagued with high switching stress, decreased efficiency and inadequate dynamic response under diverse environmental conditions. To mitigate these issues this work uses a DSCIB converter and an APO-PI controller. Proposed

10.22060/EEJ.2026.24622.5737

approach gives high voltage gain, better voltage regulation, lower overshoot and higher efficiency which makes it suitable for grid tied EVCS and smart grid applications.

### 1-1- Related Works

**Chang-Hua Lin *et al* (2024) [17]** have introduced a novel high-gain non-isolated non-CI boost converter for RES systems. It effectively boosts low DC voltage level attained from PV system to higher level, it is preferred when there is no isolation required. Though, a high-frequency transformer is employed to interrupt direct current flow, this approach results in increased system bulk and associated costs. **Yannam Ravi Sankar *et al* (2024) [18]** have implemented a crow search optimized PI controller for grid system. Crow Search Algorithm (CSA) is integrated for improving performance of PI controller, guaranteeing faster dynamic response. Nonetheless, it struggles under varying load conditions and nonlinear system behaviour. **Md. Rezanul Haque *et al* (2023) [19]** have presented a modified PI controller for achieving essential voltage and high-current density with insignificant overshoot. Modified PI controller effectively reduces conduction loss, leakage power loss and switching power loss, without neglecting switching frequency aids to preserve size of passive components. Yet, limits its scalability and real-time responsiveness in complex energy systems without the incorporation of intelligent optimization algorithms.

The novelty of this work combination of a DSCB Converter with an APO based PI controller for grid-powered solar EV charging applications. The APO algorithm offers a better exploration-exploitation tradeoff for controller parameter tuning than the existing methods based on GA, PSO, BFOA and CSA optimisation methods. This reduces overshoot, improves voltage stability, increases converter efficiency and improves system performance under steady and variable operating circumstances. The Compared existing approaches, proposed system attain higher voltage gain, lower component stress, more stable voltage regulation, lower overshoot and optimum converters efficiency under different operating condition.

10.22060/EEJ.2026.24622.5737

The proposed research contributions are listed below:

- The primary renewable energy source, PV system is utilized to effectively convert sunlight into DC power for EVCS.
- Dynamic DC power managed from PV system is boosted by DSCIB converter to a higher level with enhanced efficiency.
- The proposed boost converter is dynamically regulated by APO-based PI controller to ensure DC voltage, improving system performance under fluctuating conditions.
- BDC converter ensures controlled charging and discharging performance of EV battery.

## 2. Proposed System Description

The proposed EVCS integrated with PV system and power grid is illustrated in fig..2. The energy produced from the sun is inconsistent and fluctuating due to varying atmospheric conditions, these issues are mitigated by the proposed approach leveraging DSCIB converter with an APO- PI controller. This research enhances performance of PV-fed grid integration, assuring a stable DC power supply in EV battery management.

10.22060/EEJ.2026.24622.5737

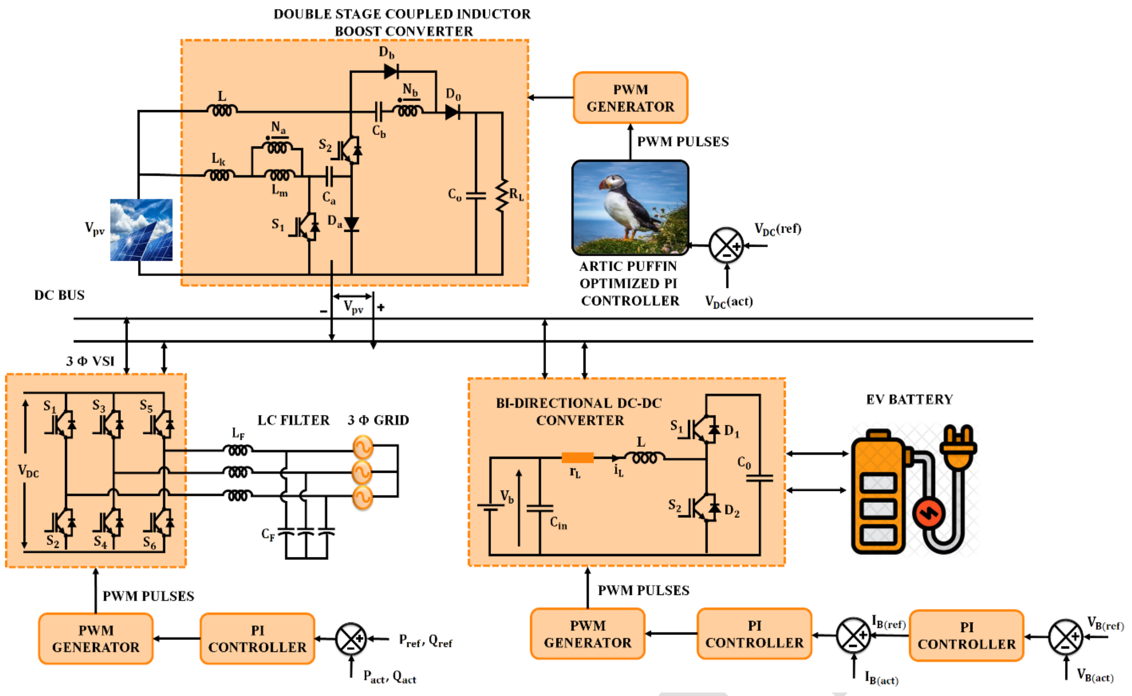


Fig. 2. Proposed PV-fed EVCS block diagram.

The PV panel, effectively converts sunlight into DC power, and it is influenced by varying ecological circumstances. To elevate the output of the system, DSCIB converter facilitates two sequential voltage boosting, where the CI improve energy conversion efficacy with decrease ripple. The converter performance effectively controlled via a PI controller. APO adjusts the controller parameters by comparing actual and reference voltage, PWM signals produced modulate converter switching operations. The boosted DC power is distributed to DC bus delivering to grid and battery system. The surplus energy generated from the PV system is transformed into AC power for grid utilization. Inverter operations are structured by a PI controller and filtered output is supplied to grid via LC filter. The enhanced DC power is delivered to the battery by a BDC converter regulating the battery charging/discharging operations, controller adjusts real-time feedback, ensuring optimal EV battery performance and longevity.

## 3. Proposed System Modelling

### 3-1- PV System

10.22060/EEJ.2026.24622.5737

PV systems offer clean energy, require minimal maintenance, operate silently, and stand out as a crucial source of renewable energy. A PV cell functions essentially as a semiconductor diode, with its p-n junction exposed to light. Performance of cell is primarily influenced by irradiation levels and temperature. Typically, the electrical behaviour of PV cell is modelled using single-diode equivalent circuit, which comprises four key elements, a photocurrent source ($I_{PH}$), a diode placed in parallel with the photocurrent source $D$, a series resistance ($R_S$), a shunt resistance ($R_{SH}$). These components work together to represent the cell's response to changing environmental conditions, as illustrated in Fig. 3.

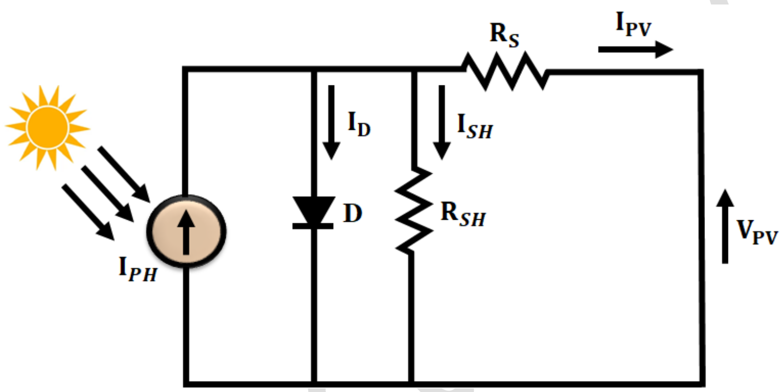


Fig. 3. Solar cell equivalent circuit.

Applying Kirchhoff's first law to current flowing through a PV cell, output current of solar cell is expressed as shown in Equation (1).

$$I = I_{PH} - I_D - I_{SH} \tag{1}$$

Here, $I$ represents output current ($A$), $I_{PH}$ denotes photo-generated current ($A$), $I_D$ refers to diode current ($A$), and $I_{SH}$ is shunt current (A). According to Shockley diode formula, current flowing via diode is given by

$$I_D = I_0\left(\exp\left[\frac{q(V + IR_S)}{mKT_C}\right] - 1\right) \tag{2}$$

Here $I_0$ denotes reverse saturation current, $q$ stands elementary charge $(1.602 \times 10^{-19}\ C)$, $K$ represents Boltzmann's constant $\left(1.380 \times 10^{-23} \frac{J}{K}\right)$, $m$ stands diode ideality factor, $T$ stands temperature in degrees Celsius, $V$ stands open-circuit voltage, and $R_S$ stands series resistance. By substituting Equation (2) into Equation (1), resulting expression is represented as Equation (3)

$$I = I_{PH} - I_0\left(exp\left[\frac{q\left(V + IR_S\right)}{mKT_C}\right] - 1\right) - \frac{V + IR_S}{R_{SH}} \tag{3}$$

These modules are further settled in series-parallel configurations to create PV arrays, enabling larger-scale power generation systems.

### 3-2- Double Stage Coupled Inductor Boost Converter

DC-DC converter intended for high step-up voltage, utilizing a double stage configuration of CI. The converter's main and secondary windings are linked in series, while the secondary winding is integrated with a voltage multiplier cell.

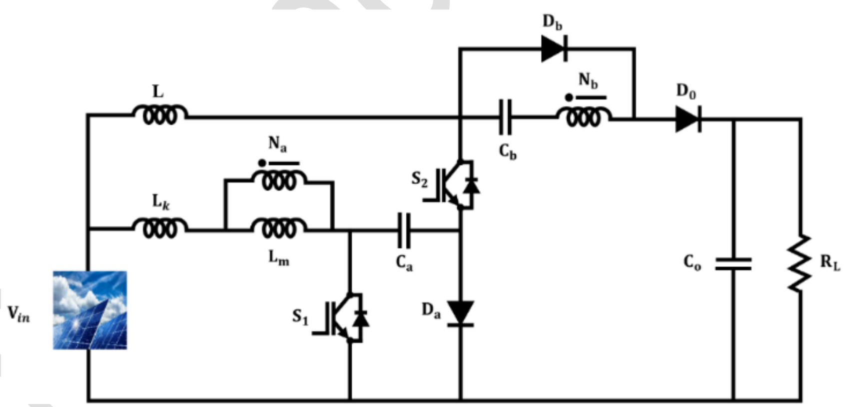


Fig. 4. Double-Stage Coupled Inductor Boost Converter.

Fig. 4 illustrates proposed converter with a DSCIB structure. Input voltage from PV source $V_{in}$ serves as the input DC power source. The first step-up stage, representing the primary quadratic unit, consists of $L, C_a$and $D_a$. Meanwhile, the second step-up stage integrates CI and voltage multiplier cell components, denoted by $N_a$ and $N_b$ and the voltage multiplier cell comprises of $N_b$, $C_b$, and $D_b$. Energy stored within the CI is transmitted to $C_0$ via diode $D_0$, which helps drive load $R_L$ and boosts output voltage.

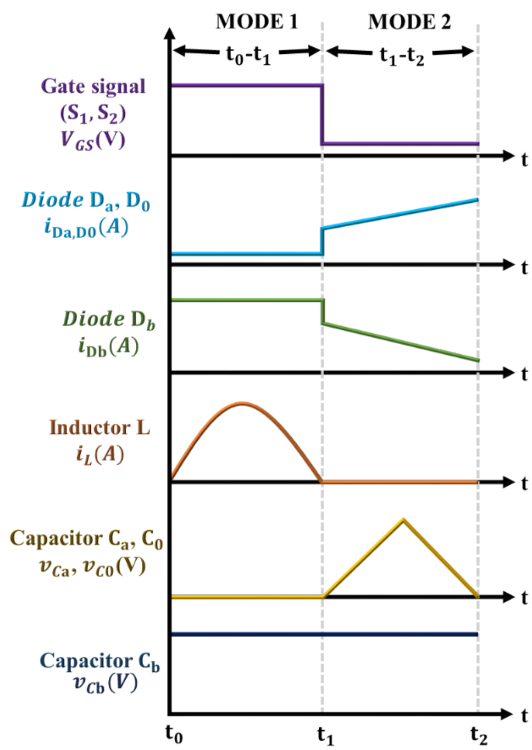


Fig. 5. Timing Diagram of DSCIB Converter.

This study explores converter's operation in continuous conduction mode, with switching cycle waveform displays in Fig.5. To streamline performance examination, the following rules are applied:

- All switches and diodes are considered ideal.
- Capacitor voltage remains constant throughout each switching cycle.
- The magnetizing inductance is sufficiently large, and the turn ratio of CI is $1\!:\!n$.

**Mode I** $(\boldsymbol{t_0 - t_1})$: From fig. 6, $S_1$ and $S_2$ are turned ON, diode $D_b$ conducts, while $D_a$ and $D_0$ remain off. $V_{in}$ energizes inductor $L$. Together with capacitor $C_a$, $V_{in}$ also supplies power to winding $N_a$ , increasing currents through magnetizing inductance $L_m$ and leakage inductance $L_k$. Since, $L_k$ voltage is negligible,

10.22060/EEJ.2026.24622.5737

it's excluded from analysis. The energy from $N_a$ is then relayed to $N_b$, which charges capacitor $C_b$. Simultaneously, output capacitor $C_0$ delivers power to the load $R_L$.

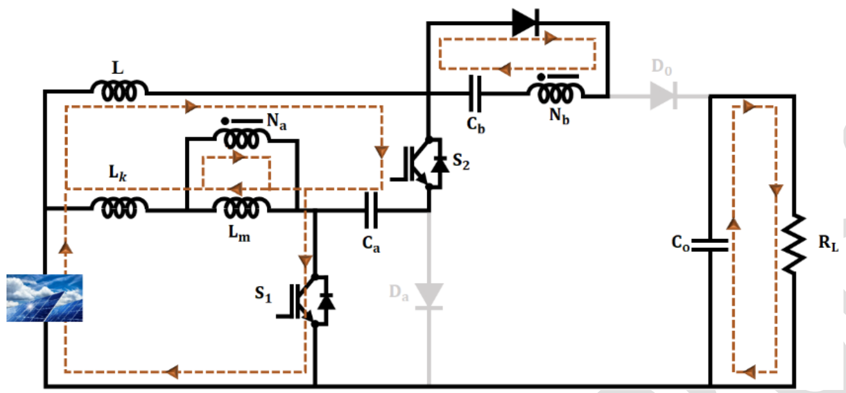


Fig. 6. Mode 1 of DSCIB Converter.

Based on KVL, the consistent equations are derived as:

$$V_{La} = V_{in} \tag{4}$$

$$V_{Lm} = V_{in} + V_{C1} \tag{5}$$

$$nV_{Lm} = V_{C2} \tag{6}$$

**Mode II ($t_1$–$t_2$):** As illustrated in Fig.7, both $S_1$ and $S_2$ are switched OFF during this interval. $D_a$ and $D_0$ are in conduction mode, while diode $D_b$ remains inactive. $V_{in}$, in conjunction with $L$, works to charge capacitor $C_a$, resulting in a reduction in $L$ current. Simultaneously, $V_{in}$ collaborates with CI and $C_b$ to supply energy to the output capacitor $C_0$.

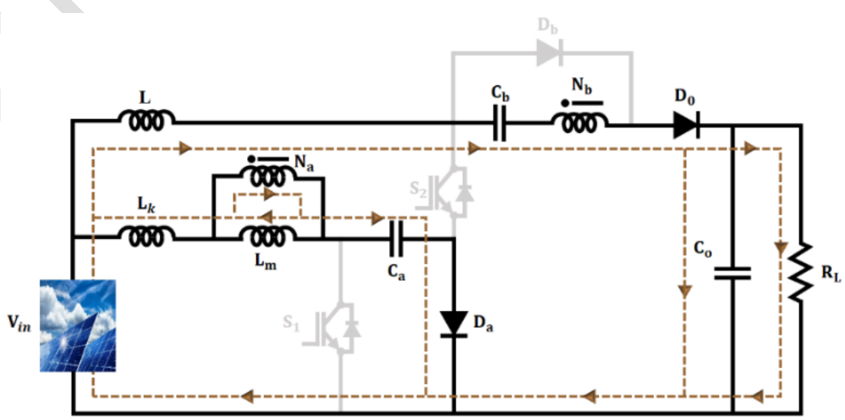

10.22060/EEJ.2026.24622.5737

Fig. 7. Mode 2 of DSCIB Converter.

The operational characteristics of this mode are described using the following mathematical expressions.

$$V_{La} = V_{in} - V_{Ca} \quad (7)$$

$$(n+1)V_{Lm} = V_{in} + V_{Cb} - V_{C0} \quad (8)$$

According to volt-second balance principle, net voltage across $L$ and $L_m$ over a switching cycle equals zero. This yields the following expressions:

$$\int_0^{DT} V_{in} dt + \int_{DT}^{T} (V_{in} - V_{Ca}) dt = 0 \quad (9)$$

$$\int_0^{DT} \frac{V_{Cb}}{n} dt + \int_{DT}^{T} \frac{V_{in} + V_{Cb} - V_{C0}}{n+1} dt = 0 \quad (10)$$

Here $D$ stands duty cycle and $T$ stands switching period. Voltage across capacitors during operation is be described as,

$$V_{Ca} = \frac{V_{in}}{1-D} \quad (11)$$

$$V_{Cb} = \frac{n(2-D)V_{in}}{1-D} \quad (12)$$

$$V_{C0} = V_0 = \frac{(2n+1-nD)V_{in}}{(1-D)^2} \quad (13)$$

The voltage gain is obtained,

$$M = \frac{V_0}{V_{in}} = \frac{2n+1-nD}{(1-D)^2} \quad (14)$$

Key benefits of this design include achieving a high voltage gain, minimizing voltage stress on switching components, ensuring continuous input current flow between power source and load.

***Converter Design Analysis***

10.22060/EEJ.2026.24622.5737

*Inductor and Capacitor Design*

The DSCIB converter's inductors and capacitors are configured to provide CCM operation and to minimize the output voltage ripple. The inductor size is specified according to current ripple ratings and switching frequency, and the output capacitor specifications are established from ripple ratings at the output. Precise sizing of these two component types increases the stability and dynamic performance of the converter. Input inductor value is determined as:

$$L = \frac{V_{in} D}{f_s \Delta I_L} \tag{15}$$

Output capacitor is similarly sized to minimize output voltage ripple, and is determined from:

$$C_o = \frac{I_o D}{f_s \Delta V_0} \tag{16}$$

Where, $\Delta V_0$ stands allowable output voltage ripple.

*Ripple analysis:*

Ripple analysis is to determine steady-state performance of proposed converter, as well as quality of output power from the converter. Inductor current ripple as a percentage is expressed as:

$$\%\Delta I_L = \frac{\Delta I_L}{I_L} \times 100 \tag{17}$$

Output voltage ripple as a percentage is expressed as:

$$\%\Delta V_0 = \frac{\Delta V_0}{V_0} \times 100 \tag{18}$$

Where $\Delta I_L$ and $\Delta V_0$ stands peak-to-peak inductor current ripple and output voltage ripple, $V_0$ stands average output voltage.

*Voltage and Current Stress Analysis*

To ensure proposed converter operates safely and reliably across a range of functioning circumstances, voltage and current stress are analysed for each of the semiconductor devices in the proposed router. Stress analysis is a key factor used in selecting the appropriate switching devices and determining their voltage and current ratings. A stress reduction help to improve converter efficiency, reliability and longevity. Maximum voltage stress across power switch is assumed via:

$$V_{stress} = V_{sw\_max} \tag{19}$$

Here $V_{sw\_max}$ stands maximum voltage. Maximum current stress flowing through the switch is given by:

$$I_{stress} = I_{sw\_max} \tag{20}$$

Here $I_{sw\_max}$ stands maximum peak current flowing over the switch at the poor power supply condition.

**3-3- Artic Optimization Based PI Controller**

The artic optimization algorithm is integrated for enhancing the PI controller performance. The proportional-integral control unit functions within a closed-loop system, eliminating the need for manual intervention. By incorporating the proportional component, it delivers a quicker response than systems using integral control alone. The feedback mechanism as exposed in Fig. 8,

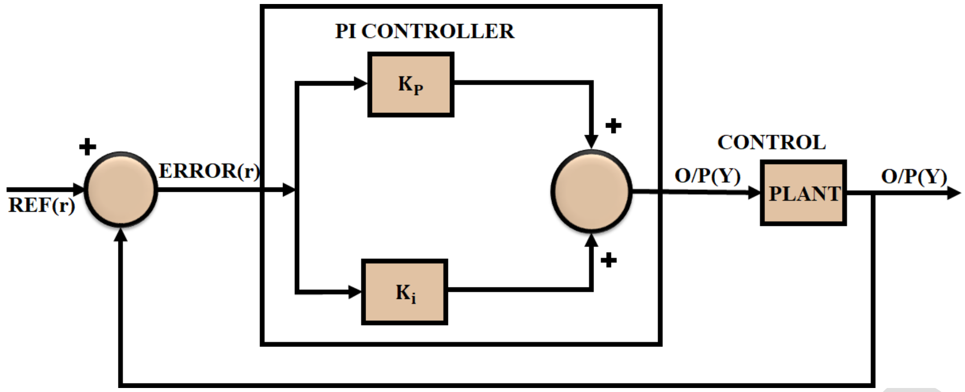


Fig. 8. PI controller.

PI control loop begins by using the output signal as feedback to continuously refine and correct performance. This feedback is compared against a reference input signal, and the difference, known as the error signal, is sent to controller for adjustment. PI control algorithm applies two main parameters: Proportional gain $(K_p)$ and Integral gain $(K_i)$. The controller output, denoted as $U(S)$ is the sum of these proportional and integral contributions, as captured in the PI control equation (21),

$$U(S) = K_p E(S) + \frac{1}{S} K_i \int E(S) \quad (21)$$

**3-3-1 Population Initialization**

Each Arctic puffin represents a candidate solution comprising a pair of $K_p$ and $K_i$ values are randomly generated within predefined bounds using the following equation,

$$X_i^t = rand \cdot (ub - lb) + lb, i = 1, 2, 3, \ldots N \quad (22)$$

Position of the $i^{th}$ puffin is $X_i^t$, corresponding to a specific combination of $K_p$ and $K_i$, $rand$ is randomly generated value uniformly distributed range in $[0, 1]$, $ub$ and $lb$ stands upper and lower bounds for PI parameters, $N$ stands total population size, i.e., the number of puffins (candidate solutions)

This randomized initialization enables diverse exploration of the search space, ensuring that the APO algorithm begins with a broad range of potential solutions for tuning the PI controller effectively.

10.22060/EEJ.2026.24622.5737

### 3-3-2 Aerial Flight Stage (Exploration)

APO algorithm applies techniques involves Lévy flight and velocity factors to update the position of each puffin (candidate solution) dynamically, enhancing the global search capability. During this stage, position update for $i^{th}$ puffin at iteration $t + 1$ is governed via the following equation (23):

$$Y_i^{t+1} = X_i^t + \left(X_i^t - X_r^t\right) \cdot L\left(D\right) + R \tag{23}$$

Where, $X_i^t$ stands current position of $i^{th}$ puffin (solution), $X_r^t$ represents the position of a randomly selected puffin from the population, $L(D)$ is a random value drawn from Lévy flight supply, which encourages long jumps for diverse exploration, $R$ is a normally distributed random variable that injects stochasticity to prevent premature convergence. This intelligent mechanism helps algorithm explore search space more thoroughly and increases likelihood of locating optimal PI controller parameters.

### 3-3-3 Merging Candidate Positions

The APO algorithm simulates a puffin's rapid dive to seize prey, mirroring how the birds transition from flight to targeted underwater hunting. This behaviour is used to refine candidate solutions during the local exploitation phase.

The updated position of each puffin is calculated using the equation (24):

$$Z_i^{t+1} = Y_i^{t+1} \cdot S \tag{24}$$

Here, $Z_i^{t+1}$, is the new position of the $i^{th}$ puffin during the exploitation step, the Puffin's position following the aerial flight stage in the exploration phase is $Y_i^{t+1}$, the velocity coefficient $S$ controls the intensity of the positional shift, simulating the puffin's swooping dive. This maneuver enhances precision in local search, enabling the algorithm to exploit capable regions of search space for fine-tuning PI controller parameters.

### 3-3-4 Underwater Foraging Stage (Exploitation)

After completing the exploration (aerial flight) and exploitation (swooping predation) phases, the APO algorithm consolidates all candidate solutions to update the population for the next iteration. This step ensures that only the fittest individual's progress. Candidate positions from both search phases are merged and ranked fitness values, and the top-performing puffins are chosen to form the new population. This process is mathematically expressed through the following equations (25):

$$P_i^{t+1} = Y_i^{t+1} \cup Z_i^{t+1} \tag{25}$$

$P_i^{t+1}$ is the combined pool of positions from exploration $\left(Y_i^{t+1}\right)$ and exploitation $\left(Z_i^{t+1}\right)$,

$$new = sort(P_i^{(t+1)}) \tag{26}$$

The pool is sorted by fitness, producing an ordered list from most to least effective candidate

$$X_i^{t+1} = new\left(1:N\right) \tag{27}$$

The top $N$ solutions are selected as the next generation, ensuring continual improvement and convergence toward optimal PI controller parameters. This strategy helps the algorithm preserve high-quality solutions while still allowing room for exploration in subsequent iterations.

*Underwater Foraging Stage (Exploitation):*

This stage mimics puffins' adaptive underwater hunting strategies to enhance the local search accuracy of the APO algorithm. It includes three coordinated mechanisms, each contributing to refined solution tuning:

1. *Gathering Foraging:* It reflects the cooperative hunting behavior of puffins, where individuals update their positions by interacting with others. The position update is governed by:

$$W_i^{t+1} = \begin{cases} X_{r1} + F \cdot L\left(D\right) \cdot \left(X_{r2} - X_{r3}\right), & if\ rand \geq 0.5 \\ X_{r1} + F \cdot \left(X_{r2} - X_{r3}\right). & if\ rand < 0.5 \end{cases} \tag{28}$$

10.22060/EEJ.2026.24622.5737

The new candidate position is $W_i^{t+1}$, co-operative factor $F$ is 0.5, levy flight distribution is $L(D)$, and the randomly selected puffin positions are $(X_{r1}, X_{r2}, X_{r3})$.

*2.* *Intensifying Search:* When food becomes scarce, analogous to poor solution quality the search becomes more aggressive and focused. This is achieved by amplifying movement around promising positions using:

$$Y_i^{t+1} = W_i^{t+1} \cdot (1 + f) \tag{29}$$

$$f = 0.1 \cdot (rand - 1) \cdot \frac{(T - t)}{T} \tag{30}$$

Here, $T$ stands total number of iterations, current iteration is $t$ and $f$ is a dynamic convergence factor that intensifies search as the algorithm progresses

*3.* *Avoiding Predators:* To preserve diversity and prevent premature convergence, puffins execute evasive maneuvers, adjusting their positions to dodge (predatory traps) in the search space:

$$Z_i^{t+1} = \begin{cases} X_i + F \cdot L(D) \cdot (X_{r1} - X_{r2}), & if\ rand \geq 0.5 \\ X_i + \beta \cdot (X_{r1} - X_{r2}) & if\ rand < 0.5 \end{cases} \tag{31}$$

Where, $\beta$ is a random variable in [0,1], adding adaptive behaviour.

10.22060/EEJ.2026.24622.5737

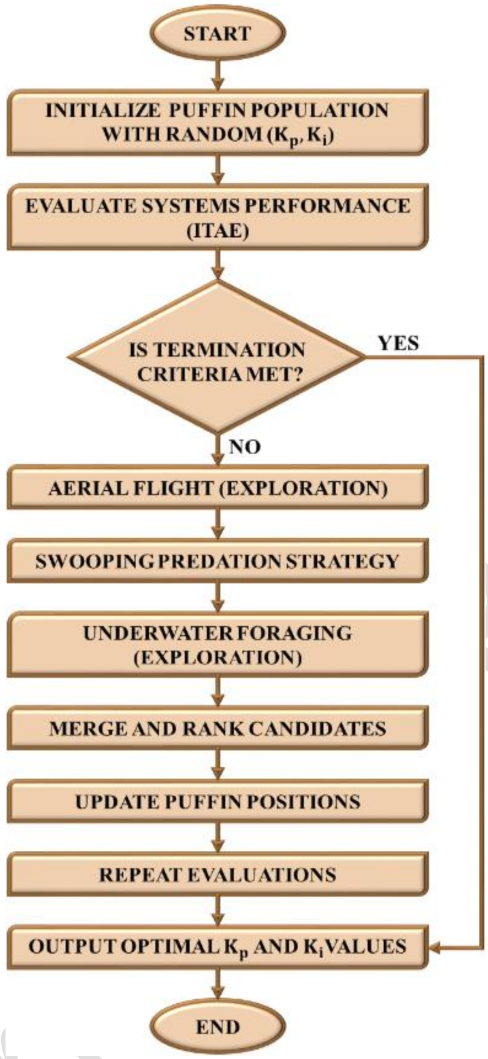


Fig. 9. Flowchart of APO.

The APO algorithm's flowchart is given in fig. 9 that effectively optimize the controller gain parameters by minimizing a specific performance index typically Integral of Time-weighted Absolute Error (ITAE) to enhance system stability and dynamic response.



**3-4- Grid Synchronization**

The 3-phase voltage source inverter comprises six actively controlled switches, which convert high-side DC voltage into a balanced three-phase (3ϕ) AC output. These switches are driven via PWM signals to ensure output voltage meets desired amplitude and frequency while minimizing harmonic distortion. PWM

10.22060/EEJ.2026.24622.5737

techniques is widely adopted due to its constant switching frequency and effective regulation of voltage magnitude and frequency. It also significantly reduces harmonic content in both current and voltage outputs and is easily implemented.

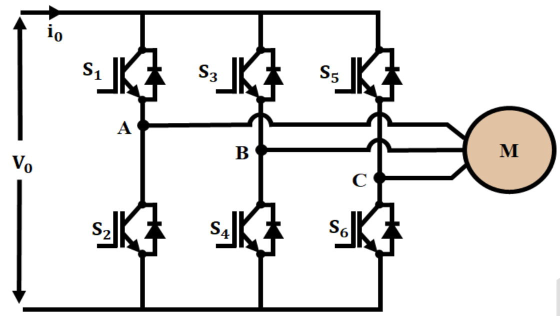


Fig. 10. 3ϕ VSI circuit diagram.

Fig. 10 illustrates circuit configuration of a 3ϕ voltage source inverter utilizing six IGBTs. The upper switches $(S_1, S_3, S_5)$ and the lower switches $(S_2, S_4, S_6)$ operate in a complementary fashion. The control strategy involves eight switching states, as visualized in Fig. 11.

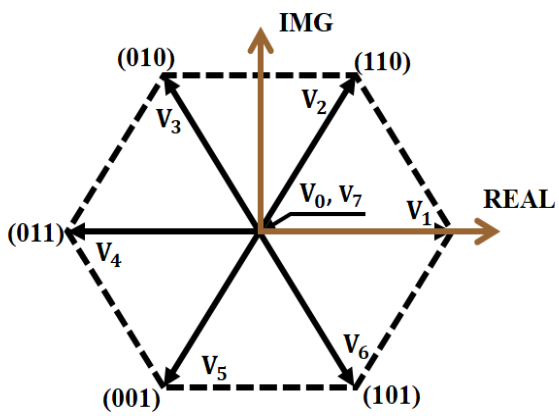


Fig. 11. 3-phase VSI voltage sectors.

These states include six active voltage vectors $(V_1)$ through $(V_6)$ spaced 60 electrical degrees apart, forming the vertices of a hexagon. Additionally, two zero voltage vectors ($V_0$ and $V_7$) reside at the origin. The inverter's phase-to-neutral voltages are then derived using the following equations:

$$V_a = \left(2Q_1 - Q_2 - Q_3\right) * V_0 / 3 \tag{32}$$

$$V_b = \left(2Q_2 - Q_1 - Q_3\right) * v_0 / 3 V_c = \left(2Q_3 - Q_1 - Q_2\right) * v_0 / 3 \tag{33}$$

These relationships ensure a balanced 3ϕ AC output suitable for grid interfacing or driving electric motors.

**3-5- Bi-Directional Converter**

BDC converter is illustrated in fig. 12, showcasing its dual-mode capability, boosting battery voltage during EV propulsion and stepping it down during regenerative braking, enabling efficient two-way power transfer between battery and DC-link.

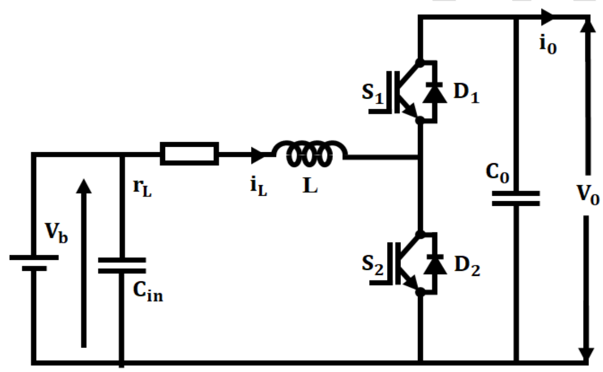


Fig. 12. Structure of BDC converter.

BDC converter comprises of two controllable $S_1$and $S_2$, $D_1$and $D_2$, $C_{in}$, $C_{out}$ and $L$ with its series resistance $r_L$. This topology ensures the converter to improves the EV battery voltage from a lower level to a higher level, making it appropriate for supplying power to the inverter and the traction motor. In reverse operation, such as during regenerative braking, the converter also function to store recovered energy back into the battery.

The two basic DC-DC converter configurations are integrated in series:

*Boost converter:* It directs power from battery to DC link in driving mode.

*Buck converter:* It transfers power from DC link to battery during regenerative braking.

Operational states are given as follows:

- Driving mode (boost): Switch $S_1$ and diode $D_2$ are active depending on the PWM signal, while $S_2$ and $D_1$ remain off.
- Regenerative mode (buck): Switch $S_2$ and diode $D_1$ are active under PWM control, while $S_1$ and $D_2$ remain off.

This system dynamically modelled by, the state vector is defined as,

$$x = \begin{bmatrix} i_L \\ v_0 \\ v_b \end{bmatrix} \tag{34}$$

Representing the inductor current $(i_L)$, output voltage $(v_0)$, and battery voltage $(v_b)$. Based on this, state-space representation of system is established,

$$x = \begin{bmatrix} -\frac{r_L}{L} & \frac{(1-D)}{L} & \frac{1}{L} \\ \frac{(1-D)}{C_0} & 0 & 0 \\ -\frac{1}{C_{in}} & 0 & 0 \end{bmatrix} x + \begin{bmatrix} 0 & 0 \\ -\frac{1}{C_0} & 0 \\ 0 & \frac{1}{C_{in}} \end{bmatrix} \begin{bmatrix} i_0 \\ i_b \end{bmatrix} \tag{35}$$

taking into account the switch duty cycle $(d)$, which equals 1 when the switch is ON and 0 when OFF. The relationship between battery voltage and output current is given by:

$$v_b i_L = v_0 i_0 \tag{36}$$

Thus, surplus energy generated from PV system is effectively delivered to battery by BDC converter for effective EV charging applications.

## 4. Result and Discussion

10.22060/EEJ.2026.24622.5737

This section discuss simulation outcomes of proposed integrated PV system for EV charging, providing insights into its performance, operational efficiency, and environmental impact, as demonstrated through MATLAB-based analysis. Design parameters utilized for system configuration are detailed in Table 1.

Table 1. Parameter Specifications

| Parameter | Specifications |
|---|---|
| **PV System** | |
| $No. of\ panels\ connected\ in\ parallel$ | 2 |
| $Open\ Circuit\ Voltage$ | $37.25V$ |
| $Rated\ Power$ | $25kW$ |
| $Short\ Circuit\ Current$ | $8.95A$ |
| $No. of\ panels\ connected\ in\ series$ | 17 |
| DSCIB converter | |
| $C_a, C_b$ | $22\mu F$ |
| Switching Frequency | $10kHz$ |
| $L, L_m, L_k$ | $4.7mH$ |
| $C_0$ | $2200\ \mu F$ |
| BDC Converter | |
| $L$ | $4.7mH$ |
| $C_0$ | $2200\ \mu F$ |
| Inverter Output Filter | |
| $L_f$ | $2-4\ mH$ |
| $C_f$ | $10-30\ \mu F$ |

**Case 1: Constant Condition**

10.22060/EEJ.2026.24622.5737

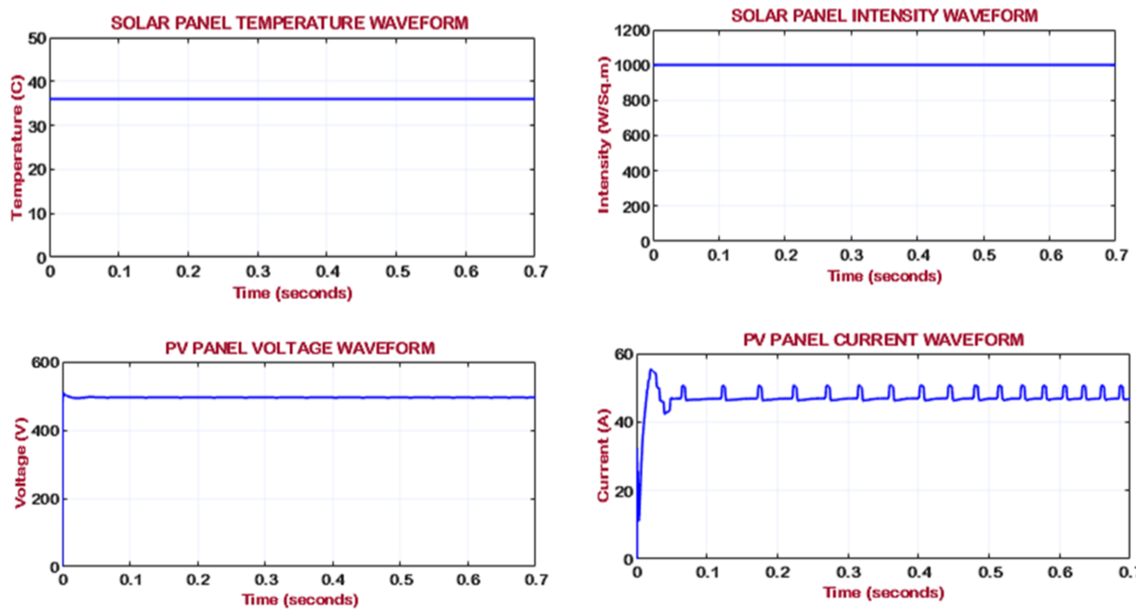


Fig. 13. PV panel waveforms (Case 1).

Fig. 13 presents PV system temperature, intensity, voltage and current under constant condition. Solar panel exhibits a continual temperature of $35^0$ C throughout the system, indicating steady environmental conditions. The PV system intensity is consistently maintained at 1000W/sq.m. for the entire system, ensuring stable solar irradiance on the PV system. From, the PV panel voltage waveform, a consistent DC voltage of $500V$ is attained. After sudden initial rise, the PV system achieves relatively stable current around $50A$ with minor fluctuations.

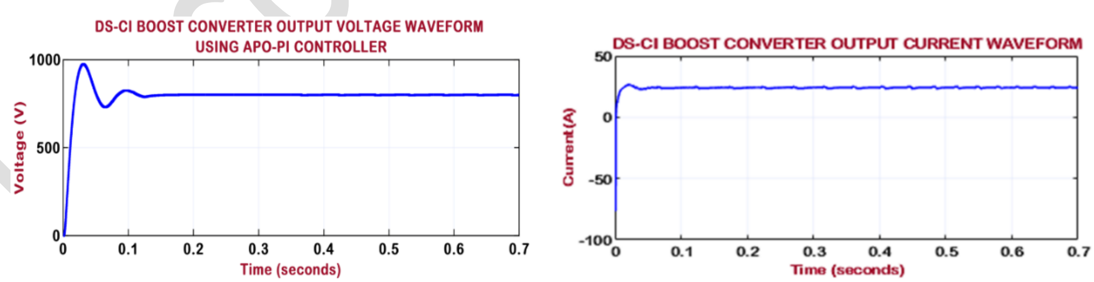


Fig. 14. DSCIB converter waveforms (Case 1).

Fig.14 represents the proposed DSCIB converter output voltage and current in constant condition. Output voltage waveform of DSCIB converter demonstrates a sudden voltage rise and then stabilize around $820V$,

10.22060/EEJ.2026.24622.5737

with little fluctuations under constant operating conditions. From the DSCIB converter, the current rapidly increases and settles around $30A$, with minimal fluctuations, indicating the controllers ability to ensure a constant output current.

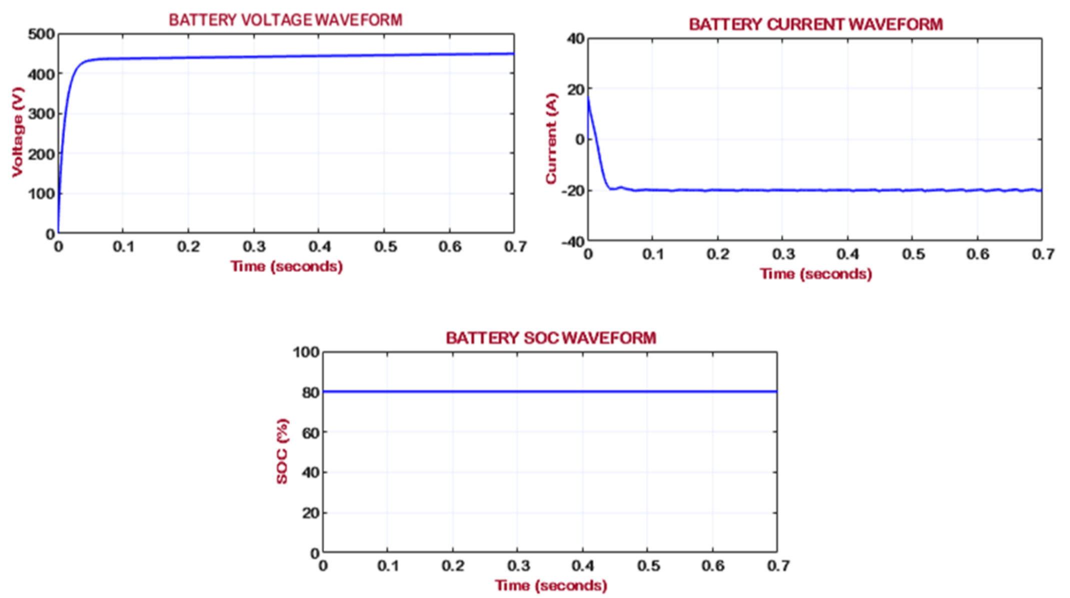


Fig. 15. SoC waveforms (Case 1).

Fig.15 illustrates the performance waveforms of a battery within a PV-fed EVCS. The battery voltage demonstrates a sudden rise during initial phase, and quickly stabilized, indicating controlled charging. The current decreases and then settles at $-20A$, ensuring current flows to the battery. SoC level of battery is preserved at $80\%$, maintain availability for EVCS.

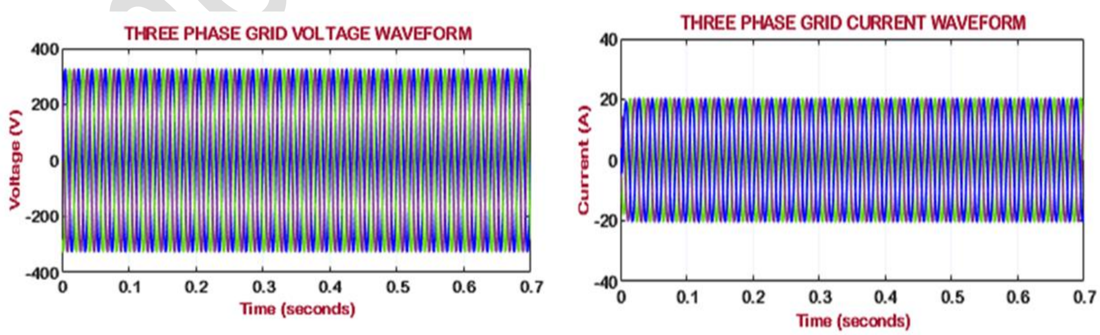


Fig. 16. 3ϕ grid waveforms (Case 1).

10.22060/EEJ.2026.24622.5737

Fig. 16 displays the voltage and current of 3ϕ grid under constant conditions. A stable sinusoidal grid voltage of $350V$ is maintained throughout the system, exhibiting constant output voltage from the PV based grid system. The consistent grid current of $20A$ is attained, demonstrating enhanced current regulation and synchronization within the grid.

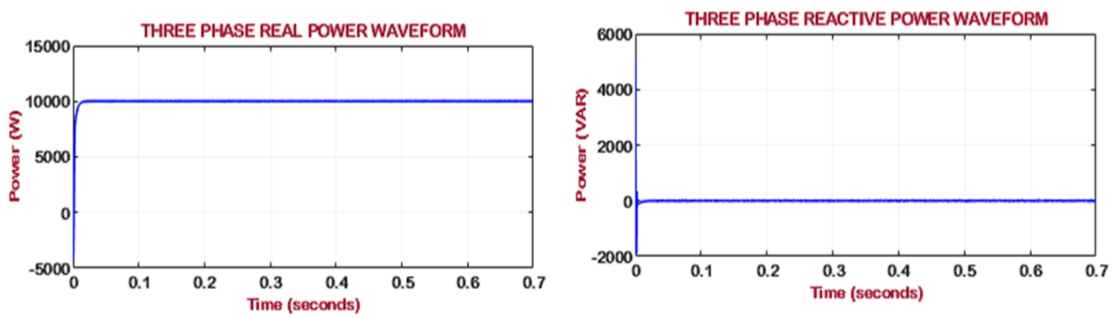


Fig. 17. Real and reactive power (Case 1).

Fig. 17 represents 3ϕ real and reactive power of PV based EVCS, after initial rise, the real power quickly stabilizes, exhibiting consistent active power to grid. From reactive power waveform, it quickly settles around zero, demonstrates system's capability to sustain a power factor close to unity at point of common coupling. Minimal reactive power output highlights successful reactive power compensation and seamless grid integration, resulting in reduced reactive flow and enhanced power quality, attained through precise converter control and a finely tuned PI controller. In this operating condition, the PV generated power is shared between the grid, EV charging load and the BESS. Therefore, the power fed to the grid represent net surplus power after meeting the EV charging demand and system losses.

**Case 2: Varying Condition**

10.22060/EEJ.2026.24622.5737

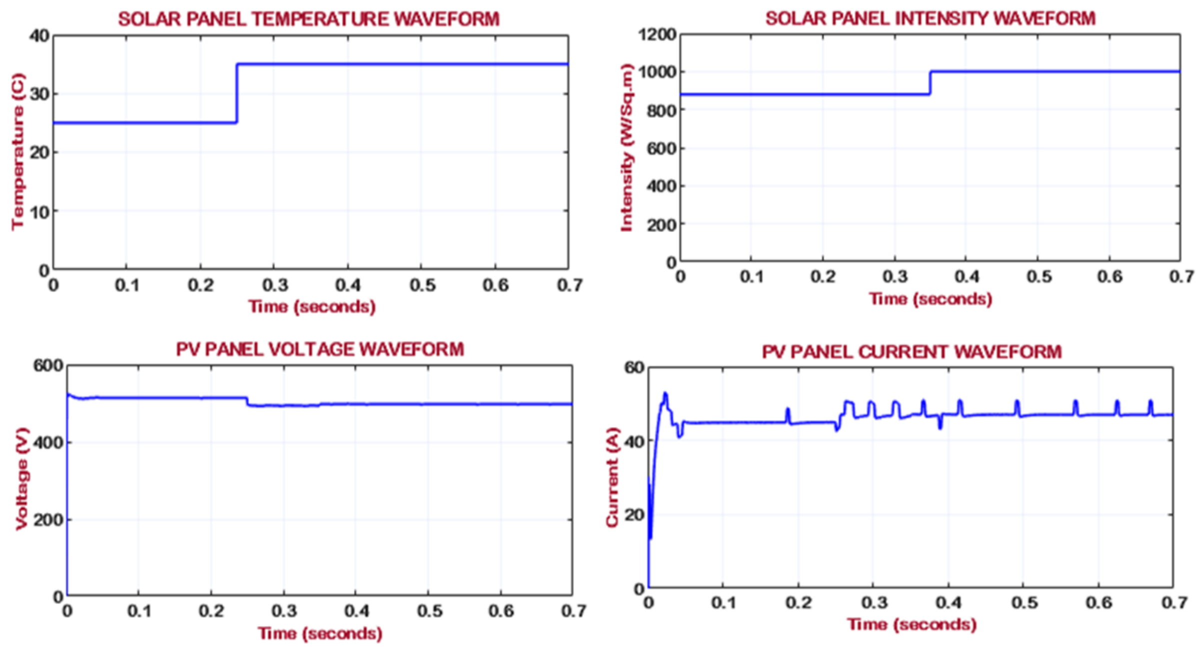


Fig. 18. PV panel waveforms (Case 2).

Fig.18 visualizes PV array temperature, intensity, voltage and current waveform under varying conditions. The temperature of the panel attains $35^0$ C after $0.3s$, indicating dynamic environmental conditions influencing PV system. The solar intensity initially remains at 850 W/sq.m. and increases to 1000W/sq.m. at $0.3s$ stays throughout the system. Output voltage of PV panel is maintained at $500V$, and drops to $470V$, due to the change in environmental conditions. At the initial fluctuations, the current of the PV panel attains $50A$ with minor fluctuations, indicating dynamic response of system.

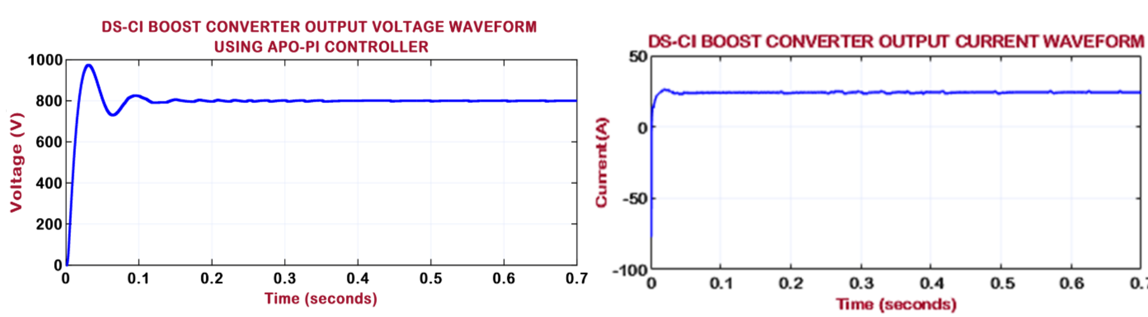


Fig. 19. Output waveform of DSCIB converter (Case 2).

10.22060/EEJ.2026.24622.5737

Fig. 19 displays output voltage and current under varying operational conditions. At initial phase, the voltage increases and stabilizes at $800V$ with transient response, attaining optimal output voltage. The current rises and settles around $25A$, ensuring power delivery to the grid for maintaining stable current supply even under fluctuations conditions.

**Case 3: PV disconnected at 0.3s grid power the system**

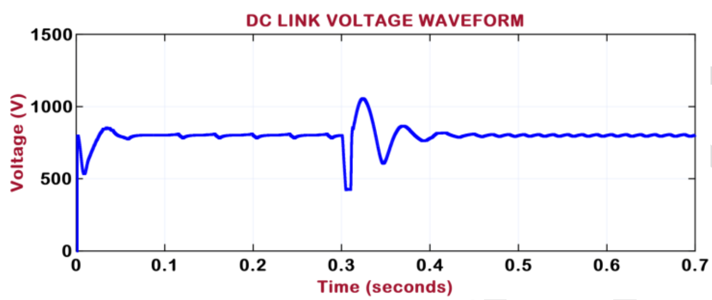


Fig.20 DC link voltage under case 3

Fig. 20 indicates voltage response of DC-link when disconnecting the PV source at 0.3 seconds. The transient voltage dip and overshoot immediately after the disturbance are due to the loss of PV output. However, the voltage quickly returns to its reference value due to the excellent ability of APO-PI controller to maintain DC-link voltage and promote stable operation of the system.

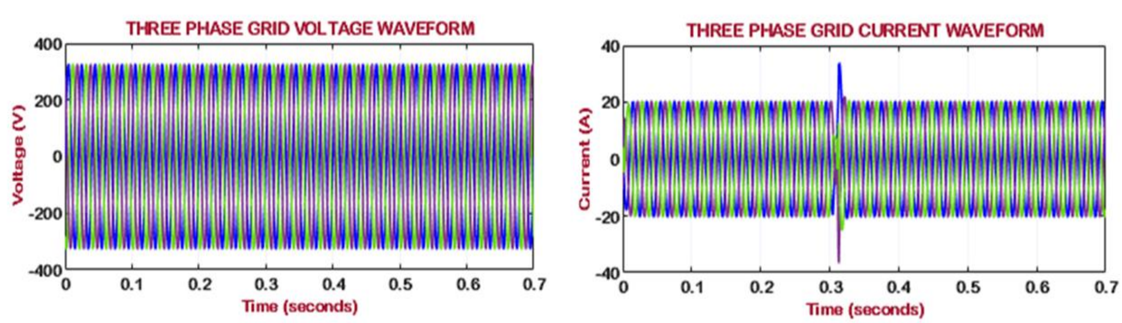


Fig. 21. 3ϕ grid system (Case 3).

Fig. 21 reveals the performance of the 3ϕ grid system during PV source disconnection at $0.3s$. The voltage waveform of the 3ϕ grid shows a continuous sinusoidal pattern, ensuring stable 3ϕ AC voltage throughout

10.22060/EEJ.2026.24622.5737

the system. The current waveform, shows a clear spike at $0.3s$, indicating PV power supply cut-off and grid performance is returning to a stable current behaviour.

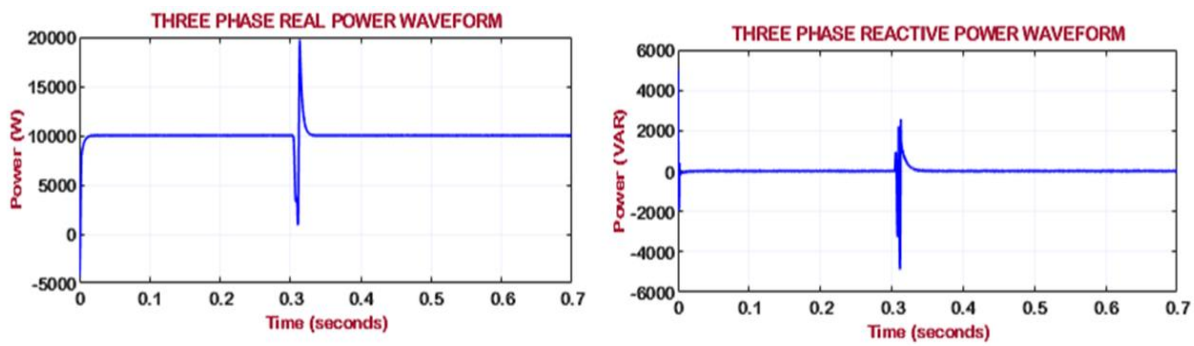


Fig. 22. Real and reactive power waveforms (Case 3).

Fig. 22 presents 3ϕ real and reactive power waveforms during condition where the PV system is disconnected at 0.3 seconds, shifting the solar EVCS to rely entirely on grid power. The real power is stable before $0.3s$, after that a brief drop followed by a recovery in real power reflects the grid compensating for the absence of PV, ensuring uninterrupted supply to the EVCS. Reactive power stays consistent until the PV disconnection at 0.3s triggers a temporary disturbance. It then quickly stabilizes as the grid takes over the reactive power load, demonstrating its capability to maintain system stability and power quality. When the PV is disconnected from the system, then the BESS must supply power to the equipment connected to the DC-link or be used to balance out a loss of power. Overall, this keep the power delivered to the grid at a constant level after a brief transient response, thereby demonstrating the effectiveness of the proposed energy management method and control system.

**Case 4: PV disconnected at 0.45s Battery powering the system**

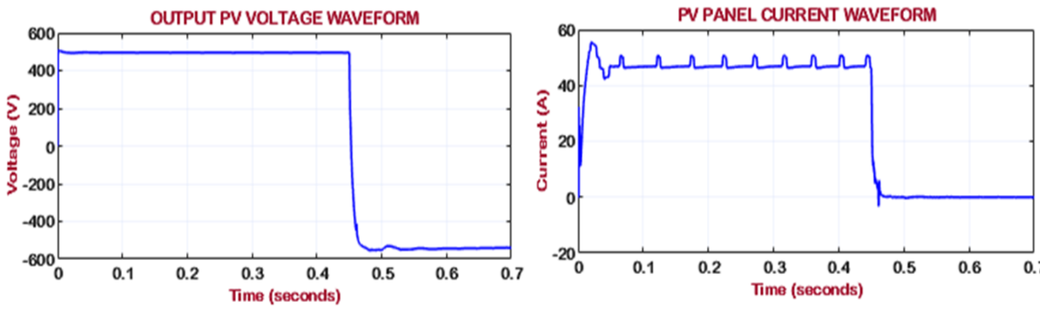


Fig. 23. PV panel waveforms (Case 4).

Fig. 23 represents the system's behaviour when the PV array is disconnected at 0.45 seconds, shifting the power source to the battery. The voltage is initially maintained around $500V$, after $0.5s$, it drops down to $-500V$, indicating battery supplying power. At initial phase, the current fluctuates and reduces after PV disconnection, ensuring battery is delivering power.

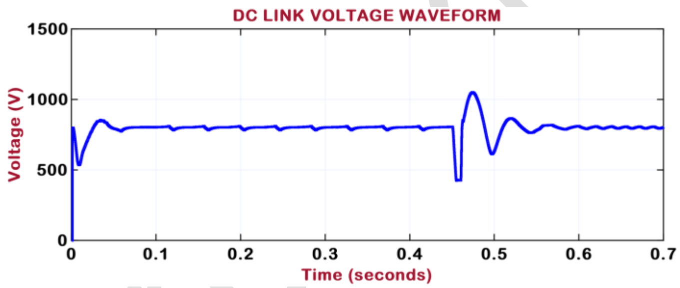


Fig.24 DC link voltage under case 4

Fig.24 shows voltage waveform of DC-link when disconnecting the PV source at 0.45 seconds. Although there is an initial fluctuation in voltage following disconnection, the controller compensates for the power unbalance very quickly and reestablishes voltage at DC-link to the reference value. This supports strong performance of proposed control methodology in the event of a PV outage.

10.22060/EEJ.2026.24622.5737

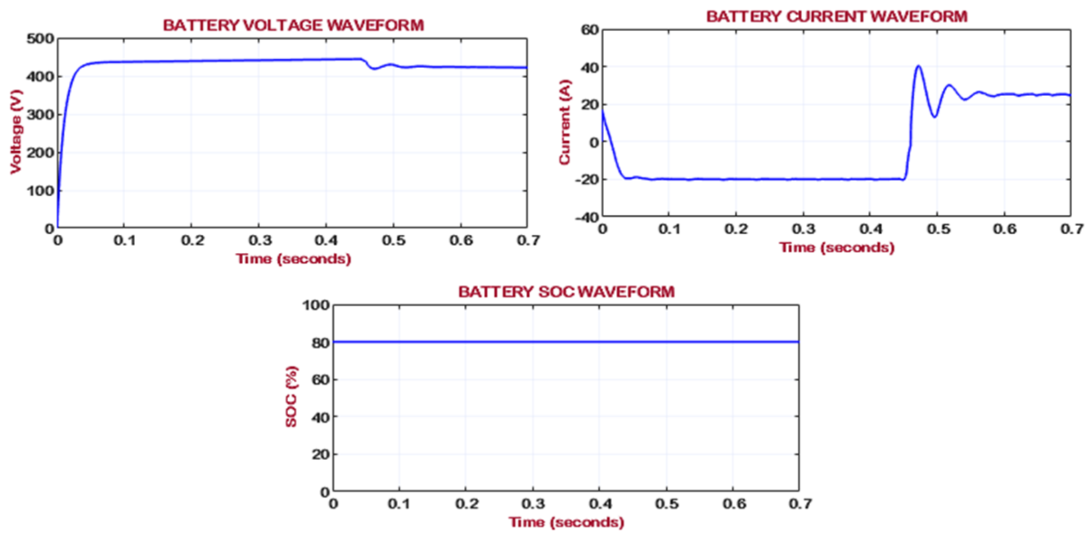


Fig. 25. Battery waveform (Case 4).

Fig. 25 displays the battery response in grid connected solar EVCS, the battery voltage is maintained around $420V$ with minimal fluctuations. Before 0.45s, current is negative $(-20A)$, implying charging, after $0.4s$, the current settles around $25A$, indicating the battery instantly begins discharging to meet system demands. SOC stays steady at around 80% throughout, even after PV disconnection. This reflects strong energy management and confirms the battery's capacity to handle the load efficiently without significant depletion.

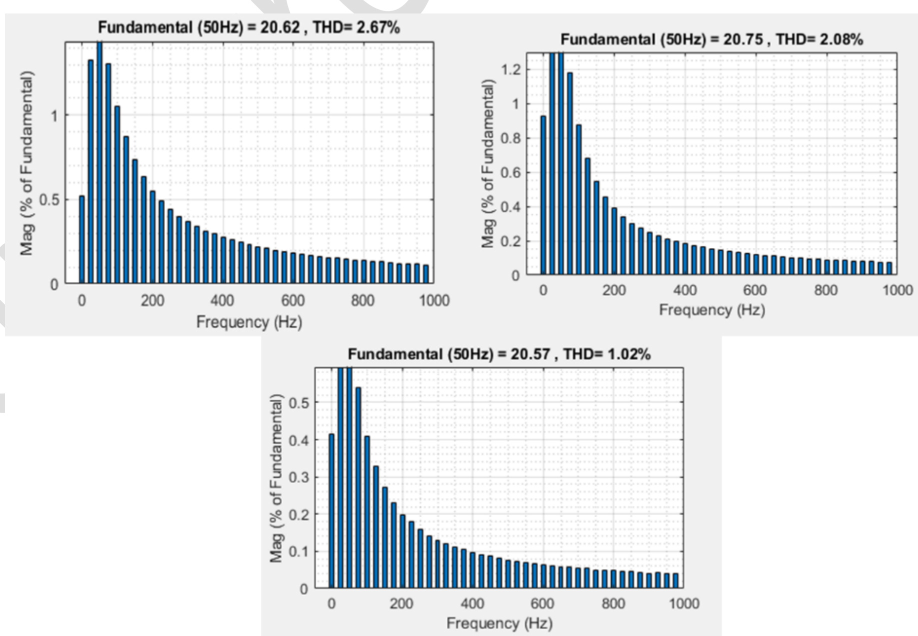

10.22060/EEJ.2026.24622.5737

Fig. 26. THD waveforms

Fig. 26 presents the total harmonic distortion waveforms across the 3ϕ grid. R phase registers a THD of 2.67%, the Y phase shows 2.08%, and the B phase achieves the lowest at 1.02%. These results highlight successful harmonic suppression, with all phases exhibiting minimized distortion, thereby improving the efficiency and performance of PV connected grid applications.

*Converter Loss and Efficiency Analysis:*

To assess efficiency of DSCIB converter, evaluate major sources of power loss including t conduction losses of both switches and diodes, the winding copper losses of CI, and the losses associated with the ESR of the capacitors. The total converter losses are signified as:

$$P_{loss} = P_{switch} + P_{diode} + P_{copper} + P_{ESR}$$

Here, -$P_{switch}$ denotes conduction losses and switching losses of power switch, $P_{diode}$ denotes conducting losses of diode, $P_{copper}$ are the windings copper losses in the inductors, $P_{ESR}$ stands equivalent series resistance of capacitors causing inefficiencies due to resistance. The efficiency is calculated by applying the following formula:

$$\eta = \frac{P_{out}}{P_{in}} \times 100$$

$$\eta = \frac{24.6kW}{25kW} \times 100$$

$$= 98.4\%$$

Where, $P_{in}$ and $P_{out}$ stands input and output power.

10.22060/EEJ.2026.24622.5737

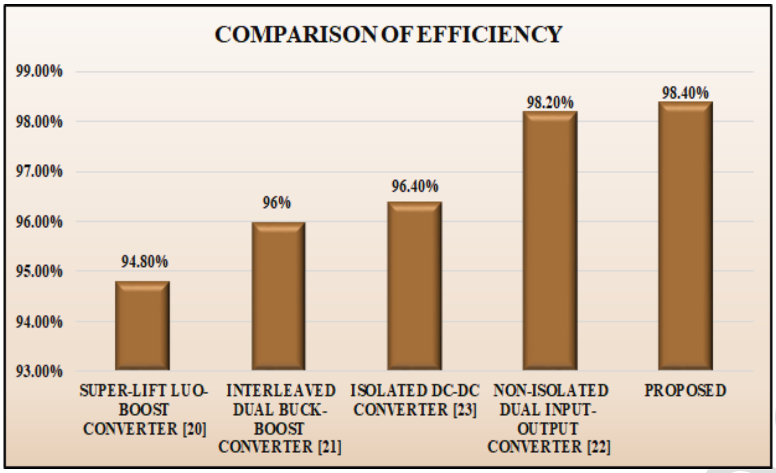


Fig. 27. Comparison of converter efficiency.

Fig. 27 compares the efficiency of various converter topologies for grid-integrated solar EV charging, where the DSCIB converter with arctic puffin optimized pi control achieves the highest efficiency (98.40%), outperforming other converter designs such as Super-Lift Luo-Boost Converter [20] at 94.80%, Interleaved Dual Buck-Boost Converter [21] at 96%, Isolated DC-DC Converter [23] at 96.40%, and Non-Isolated Dual Input-Output Converter [22] at (98.20%), emphasizing its potential for superior energy utilization and reduced losses.

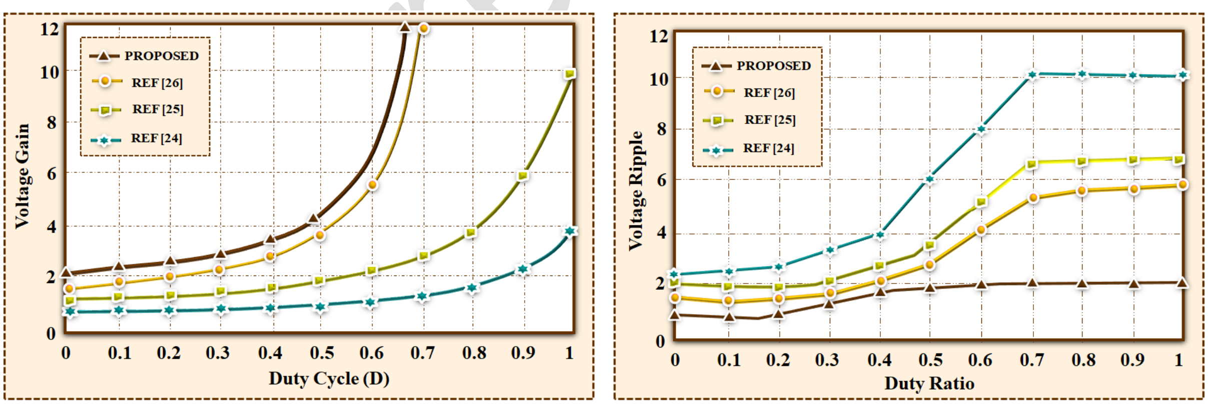


Fig. 28. (a) Voltage gain (b) Voltage ripple.

Fig. 28 displays voltage gain and voltage ripple across various converter topologies. DSCIB converter attains a notably enhanced voltage gain and low ripple voltage underscoring its superior performance. This value surpasses those recorded for previously reported designs, including the Quadratic boost converter

[26], Non-isolated high gain quadratic boost converter [25], and High-gain Transformerless DC/DC boost converter system [24], highlighting its proposed converter effectiveness in delivering a more improved power signal relative to other benchmarked topologies

Table 2. Loss Breakdown.

| Power Losses | Switch | Diode | Capacitor | Inductor |
|---|---|---|---|---|
| Isolated DC-DC Converter [23] | 1.4% | 0.9% | 0.8% | 0.5% |
| Non-isolated high gain quadratic boost converter [25] | 2% | 4% | 1% | 1% |
| Proposed | 0.7% | 0.4% | 0.3% | 0.2% |

Table.2 demonstrates power losses across various DC-DC converter topologies, outlines percentage of losses in key components such as Switch, Diode, Capacitor, and Inductor for the converter types: Isolated DC-DC [23], Non-isolated high gain quadratic boost [25], and DSCIB converter. Proposed system exhibits lowest power losses across all components, with 0.7% in the Switch, 0.4% in the Diode, 0.3% in the Capacitor, and 0.2% in the Inductor, clearly outperforming the others and underscoring its efficiency for EV charging applications.

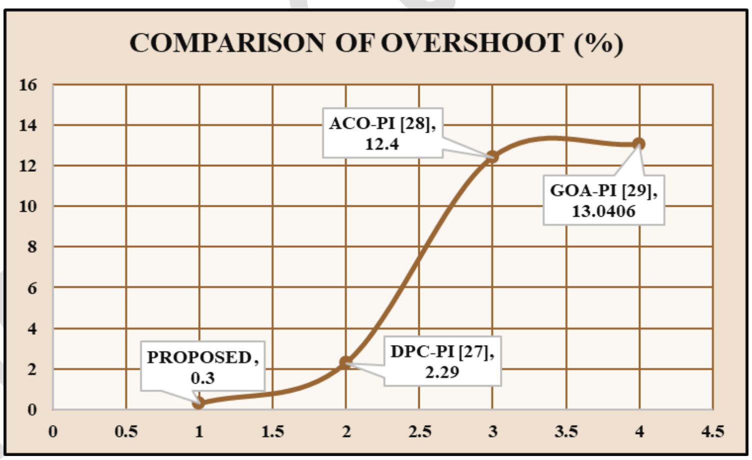


Fig. 29. Comparison of overshoot (%).

Fig. 29 signify comparative examination of overshoot for different control techniques used in a grid-connected solar EVCS. It shows the performance of the proposed arctic puffin optimized PI control, which achieves a very low overshoot of 0.3%, outperforming other techniques such as Direct Power Control (DPC)-PI [27] (2.29%), Ant Colony Optimized (ACO)-PI [28] (12.4%), and Grasshopper Optimized

10.22060/EEJ.2026.24622.5737

Algorithm (GOA)-PI [29] (13.0406%). The lower overshoot ensures a better transient response and higher stability, which are critical in maintaining efficient and reliable operation under dynamic operating conditions.

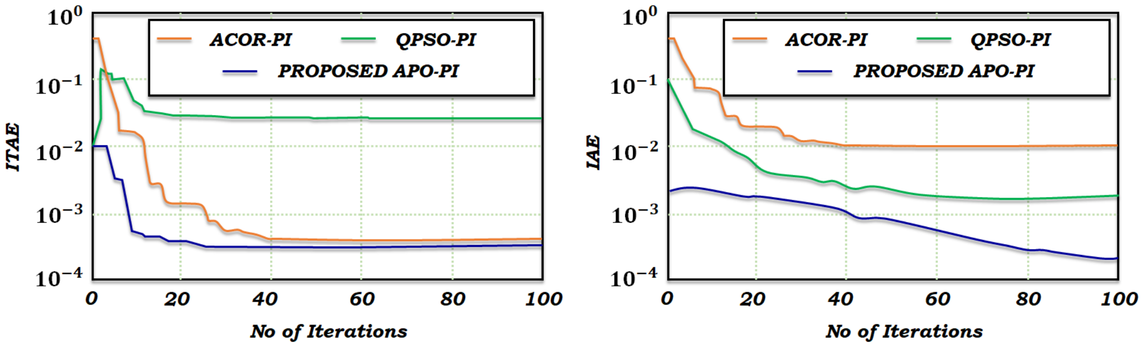


Fig. 30 Comparison of ITAE and IAE

The performance indices IAE and ITAE are compared for existing controllers as displays Fig. 30 such as ACOR-PI [30] and QPSO-PI [31] and proposed APO-PI, where the APO-PI controller provides a better error minimization and dynamic performance by successfully optimizing the PI controller parameters for the proposed charging system of PV-EV.

## 5. Conclusion

This research presents a forward-thinking to tackling the growing energy demands driven by EV adoption through integration of solar energy for charging infrastructure. The utilization of sustainable PV powered by a DSCIB converter and enhanced via an arctic puffin optimized PI control technique, demonstrates high energy conversion efficiency for solar power optimization. APO-PI controller ensures voltage stability in the energy generation system, while the grid plays a key role in balancing grid load during peak times. Simulation results in MATLAB validate the system's high efficacy at 98.4% and low THD at 1.02%, affirming the proposed solution's effectiveness. This research marks a significant step toward advancing clean transportation and robust energy management strategies for a sustainable future. The proposed APO-PI controlled DSCIB converter has demonstrated better performance yet the study is limited to simulation and does not consider practical issues such as partial shading, communication delays and real-time implementation constraints. Future work will include validation on hardware, testing on different operating conditions, and development of hybrid APO–machine learning optimisation strategies to improve system adaptability and robustness.

## REFERNCE

[1] V. Veerasamy, N.I. Abdul Wahab, A. Vinayagam, M.L. Othman, R. Ramachandran, A. Inbamani and H. Hizam, "A novel discrete wavelet transforms based graphical language classifier for identification of high impedance fault in distribution power system", 2020 International Transactions on Electrical Energy Systems, vol. 30, no. 6, pp. e12378.

[2] B. Gunapriya, I. Abinaya, M. Karthik, H. Vidhya, "Anti wind up PI controller with tracking for motor drive system: Modelling, simulation and implementation in lab view based FPGA", 2020 International Journal of Recent technology and Engineering, vol. 8, no. 5.

[3] I. Abinaya, R. R. Gandhi, H. Vidhya, M. Karthik, R. Thangaraj, "Demand Side Management for Motoring and Lighting Loads", International Journal of Research in Engineering, Science and Management.

[4] M.Z. Islam, M.L. Othman, N.I. Abdul Wahab, V. Veerasamy, S.R. Opu, A. Inbamani and V, "Annamalai, Marine predators algorithm for solving single-objective optimal power flow", 2021 PLoS One, vol. 16, no. 8, pp. e0256050.

[5] A. Watil, and H. Chojaa, "Enhancing grid-connected PV-EV charging station performance through a real-time dynamic power management using model predictive control", 2024 Results in Engineering, vol. 24, pp. 103192.

[6] S. Cheikh-Mohamad, M. Sechilariu, F. Locment and Y. Krim, "Pv-powered electric vehicle charging stations: Preliminary requirements and feasibility conditions", 2021 Applied Sciences, vol. 11, no. 4, pp. 1770.

10.22060/EEJ.2026.24622.5737


[7] D.S. Abraham, B. Chandrasekar, N. Rajamanickam, P. Vishnuram, V. Ramakrishnan, M. Bajaj, M. Piecha, V. Blazek and L. Prokop, “Fuzzy-based efficient control of DC microgrid configuration for PV-energized EV charging station”, 2023 Energies, vol. 16, no. 6, pp. 2753.

[8] C. Restrepo, B. Barrueto, D. Murillo-Yarce, J. Muñoz, E. Vidal-Idiarte and R. Giral, “Improved model predictive current control of the versatile buck-boost converter for a photovoltaic application”, 2022 IEEE Transactions on Energy Conversion, vol. 37, no. 3, pp. 1505-1519.

[9] K. S. Kavin, P. Subha Karuvelam, N. Kumar, S. Kar, R. A. Rahiman and S. Patwa, “Coupled inductor interleaved boost converter with ANN and RNN based MPPT algorithm for PV system”, 2024 International Journal of Applied Power Engineering (IJAPE), vol. 13, no. 3, pp. 616-627.

[10] N. Surulivel, D. Debnath and C. Chakraborty, “A novel single coupled-inductor boost TPC with two inductively interfaced ports suitable for renewable energy integration”, 2022 IEEE Transactions on Industrial Electronics, vol. 70, no. 5, pp. 4705-4715.

[11] G. Rajendran, C.A. Vaithilingam, N. Misron, K. Naidu and M.R. Ahmed, “Voltage oriented controller based vienna rectifier for electric vehicle charging stations”, 2021 IEEE Access, vol. 9, pp. 50798-50809.

[12] Y. Jang, Z. Sun, S. Ji, C. Lee, D. Jeong, S. Choung and S. Bae, “Grid-connected inverter for a PV-powered electric vehicle charging station to enhance the stability of a microgrid”, 2021 Sustainability, vol. 13, no. 24, pp. 14022.

[13] J. Liu, Z. Liu and H. Su, “Passivity-based PI control for receiver side of dynamic wireless charging system in electric vehicles”, 2021 IEEE Transactions on Industrial Electronics, vol. 69, no. 1, pp. 783-794.

[14] H. Wang, S. Xu and H. Hu, “PID controller for PMSM speed control based on improved quantum genetic algorithm optimization”, 2023 IEEE Access, vol. 11, pp. 61091-61102.

[15] F. Dubuisson, M. Rezkallah, H. Ibrahim and A. Chandra, "Real-time implementation of the predictive-based control with bacterial foraging optimization technique for power management in standalone microgrid application", 2021 Energies, vol. 14, no. 6, pp. 1723.

[16] C.L. Zhang, X.Z. Wu and J. Xu, "Particle swarm sliding mode-fuzzy PID control based on maglev system", 2021 IEEE Access, vol. 9, pp. 96337-96344.

[17] C.H. Lin, M.S. Khan, J. Ahmad, H.D. Liu and T.C. Hsiao, "Design and analysis of novel high-gain boost converter for renewable energy systems (RES)", 2024 IEEE access, vol. 12, pp. 24262-24273.

[18] Y.R. Sankar and K.C. Sekhar, "Hybrid PV/fuel cell based system using integrated SEPIC-Cuk converter with crow search optimized PI controller", 2024 Int. J. Power Electron. Drive Syst. (IJPEDS), vol. 15, no. 3, pp. 1726-1738.

[19] M.R. Haque, K.M.A. Salam, and M.A. Razzak, "A modified PI-controller based high current density DC–DC converter for EV charging applications", 2023 IEEE Access, vol. 11, pp. 27246-27266.

[20] R. Gopalasami, B. Chokkalingam, and S. Muthusamy, "A novel method for hybridization of super lift luo converter and boost converter for electric vehicle charging applications", 2023 Energy Sources, Part A: Recovery, Utilization, and Environmental Effects, vol. 45, no. 3, pp. 8419-8437.

[21] S. Krithiga, N. Sujitha, G.J.S.M. Sandeep, R. Gokulnath and P.S. Subudhi, "FLC-based, PV-fed interleaved dual buck-boost converter for EV battery charging applications", 2022 Heliyon, vol. 8, no. 4.

[22] K. Suresh, C. Bharatiraja, N. Chellammal, M. Tariq, R.K. Chakrabortty, M.J. Ryan and B. Alamri, "A multifunctional non-isolated dual input-dual output converter for electric vehicle applications", 2021 IEEE Access, vol. 9, pp. 64445-64460.

[23] D. Krishnan Nair, K. Prasad and T.T. Lie, "Design of a PV-fed electric vehicle charging station with a combination of droop and master-slave control strategy", 2023 Energy Storage, vol. 5, no. 5, pp. e442.

[24] H.Y. Ahmed, O. Abdel-Rahim and Z.M. Ali, “New high-gain transformerless DC/DC boost converter system”, 2022 Electronics, vol. 11, no. 5, pp. 734.

[25] S.V.K. Naresh, S. Peddapati and M.L. Alghaythi, “Non-isolated high gain quadratic boost converter based on inductor’s asymmetric input voltage”, 2021 IEEE Access, vol. 9, pp. 162108-162121.

[26] H. Tekin, K. Bulut and D. Ertekin, “A novel switched-capacitor and fuzzy logic-based quadratic boost converter with mitigated voltage stress, applicable for DC micro-grid”, 2022 Electrical Engineering, vol. 104, no. 6, pp. 4391-4413.

[27] H. Benbouhenni, I. Colak, N. Bizon, M.I. Mosaad, and T.G. Tella, “Power regulation of variable speed multi rotor wind systems using fuzzy cascaded control”, 2024 Scientific Reports, vol. 14, no. 1, pp. 16415.

[28] R. Singh and B. Bhushan, “Improved ant colony optimization for achieving self-balancing and position control for balancer systems”, Journal of Ambient Intelligence and Humanized Computing, vol. 12, no. 8, pp. 8339-8356.

[29] M.A.L. Khaniki, M.B. Hadi, and M. Manthouri, “Tuning of novel fractional order fuzzy PID controller for automatic voltage regulator using grasshopper optimization algorithm”, 2021 Majlesi Journal of Electrical Engineering, vol. 15, no. 2, pp. 39-45.

[30] Shagor, Md Rafid Kaysar, Samiur Rahman Sami, Mirza Muntasir Nishat, Fahim Faisal, Md Safwan Zaman, and Zubayer Ahmed. "Studying the Applicability of Swarm Intelligence in Designing Optimized PI Controller for DC-DC Zeta Converter: A MATLAB-Based Approach." Mathematical Problems in Engineering 2022, no. 1 (2022): 5816393.

[31] Perkasa, Sigit Dani, Prisma Megantoro, and Senit Araminta Jasmine. "Quantum-behaved particle swarm optimization-tuned PI controller of a SEPIC converter." Control Systems and Optimization Letters 3, no. 2 (2025): 144-150.